JMEPEG
https://doi.org/10.1007/s11665-020-04952-1

1059-9495/$19.00

In Vitro Corrosion Behavior and Cytotoxicity of Polycaprolactone–Akermanite-Coated Friction-Welded Commercially Pure Ti/AZ31 for Orthopedic Applications

Mojtaba Sadeghi Gogheri, Masoud Kasiri-Asgarani, Hamid Reza Bakhsheshi-Rad, Hamid Ghayour, and Mahdi Rafiei

(Submitted February 14, 2020; in revised form June 13, 2020)

This study deals with the corrosion and bioactivity behavior of biodegradable friction-welded CP-Ti/AZ31 joints. The investigations were carried out on the bare, PCL-coated and PCL–akermanite (AKT)-coated joints immersed in simulated body fluid. The samples were subjected to polarization and impedance corrosion tests, weight loss and pH monitoring and cytotoxicity investigations as well as cell adhesion test. The results of corrosion tests and weight loss measurements indicated that whereas the bare alloy shows the highest corrosion rate through 7 days (15.945 mm/y), the PCL–AKT-coated sample presented significantly improved results, even when the soaking period was prolonged to 30 days. The PCL–AKT-coated sample also showed the best biocompatibility, as the cell viability was measured to be 97.52%. The Ca/P ratio was also measured to be about 1.64 for PCL–AKT-coated sample, indicating favorable osteogenic behavior. The results of alizarin red cell staining and absorption spectrum as well as alkaline phosphatase activity confirmed superior osteogenic behavior of the PCL–AKT-coated sample. It was found that the CP-Ti/AZ31 samples coated with PCL–AKT obtained suitable corrosion resistance and cellular response, thus presenting a good potential to be used in orthopedic applications.

Keywords biodegradability, corrosion behavior, CP-Ti-AZ31, friction welding, PCL–AKT coating

1. Introduction

Magnesium-based alloys seem to be promising candidates for orthopedic implant applications, due to their low Young's modulus ($<$ 37.5-65 GPa) and mechanical properties compatible with the natural bone tissue, which can lead to decreased stress shielding effect as well as osteolysis (Ref 1-4). Biodegradability is the most appealing feature of the Mg-based implants, which makes them suitable candidates for bone implants, particularly as no second (implant withdrawal) surgery would be needed (Ref 5-7). Commercially pure Ti (CP-Ti) and Ti-6Al-4V alloys were employed for orthopedic and dentistry applications owing to their great biocompatibility and mechanical stability (Ref 8). Due to these great properties of pure Ti and Ti-6Al-4V alloys, the dissimilar welding of Ti alloy to other metallic medical materials received great attention. Friction welding (Ref 9), brazing (Ref 10-15) and diffusion bonding (Ref 16-18) are used in the dissimilar joints of titanium to other materials.

Mojtaba Sadeghi Gogheri, Masoud Kasiri-Asgarani, Hamid Reza Bakhsheshi-Rad, Hamid Ghayour, and **Mahdi Rafiei**, Advanced Materials Research Center, Department of Materials Engineering, Najafabad Branch, Islamic Azad University, Najafabad, Iran. Contact e-mails: m.kasiri.a@gmail.com, m.kasiri@pmt.iaun.ac.ir, rezabakhsheshi@gmail.com, and rezabakhsheshi@pmt.iaun.ac.ir.

Besides their potential applications as biomaterials, dissimilar weld joints of Ti and Mg alloys are an interesting subject for automotive applications (Ref 19). However, significant differences between the physical characteristics of the mentioned metals (Ti and Mg) including heat conductivity (Ti: 2.9 W m^{-1} k^{-1}, Mg: 156 W m^{-1} k^{-1}), melting point (Ti: 1668 °C, Mg: 650 °C), low mutual solubility and consequent poor reaction layers as well as unavailability of proper metal fillers challenge the Ti/Mg joining via the common fusion welding method (Ref 19, 20). To address this issue, friction welding is a solid-state welding approach that creates heat and plasticity through compressing the rotating (or relatively rotating) workpieces to each other and, consequently, promotes the workpieces to join (Ref 21-26). In spite of their advantages, the main issue of Mg alloys is concerned with their high degradation rate in wet environments (Ref 27-29). To solve this issue, surface treatments and coatings have been considered as the key solutions, which can provide barriers between the implant and the corrosive body fluid and retard the biodegeneration of the material (Ref 30-34). In this context, compared to metallic and/or ceramic coatings, biodegradable polymer coatings present advantages such as simple synthesis routes and biocompatibility (adjustment with the host tissue) (Ref 35-38). The harmful by-products of biodegradable polymers are also removed via citric acid cycle in the human body (Ref 32). Polycaprolactone (PCL), a semicrystalline polyester which is obtained through ring-opening polymerization (ROP) of monomers, offers a unique combination of properties (Ref 39-41). The material was also approved by FDA due to its stability in the human body, which provides it with the possibility of drug release in a period of 1 year (Ref 42), whereas polymer has also presented proper mechanical and bioactivity properties when applied on the Mg alloy surface (Ref 43, 44). Therefore, it is currently considered as a promising candidate for repairing the unloaded human bones.

Published online: 26 August 2020

Akermanite (AKT; $Ca_2MgSi_2O_7$) is a triple-oxide ceramic (Ca, Mg, Si), which seems to be a potentially favorable material for repairing the bone tissue, as it shows proper mechanical properties and controllable biodegradability (Ref 45). Besides its biocompatibility, AKT presents optimal chemical and mechanical stability. It has been found to enhance osteoblast cell adhesion and viability, since it releases the Si and Ca ions that promote the synthesis of hydroxyapatite and bone mineralization (Ref 46). Moreover, AKT promotes osteogenic differentiation of osteoblasts, bone marrow stroma cells (BMSCs) and adipose-derived stem cells (ASCs) (Ref 47). However, there is no comprehensive study regarding assessment of different coating strategies on corrosion and cellular response of CP-Ti/AZ31-friction-welded joints.

2. Materials and Methods

2.1 Materials and the Welding Process

In this study, CP-Ti (99.9%) and AZ31 Mg alloy rods with a nominal composition of Mg-3 wt.% Al-1 wt.% Zn, 20 mm diameter and 80 mm length (Timet Co.) were used as the raw materials. The cross sections of the rods were mechanically polished by using the 800 grit and washed using acetone in the pre-treatment steps. The friction welding process was then carried out using a continuous welding machine at a 1300 rpm rotating speed. The process parameters including the friction pressure of 50 MPa, forging pressure of 40 MPa, friction time of 4 s and forging time of 8 s were applied. The workpieces assembly and the weld joint are presented in Fig. 1(a) and (b). The samples (1 × 1 cm) were then cut from the joint and prepared for further examinations (Fig. 1c).

2.2 Coating Process

PCL precursor (Sigma-Aldrich, average Mn of 80000) was initially solved in dichloromethane via a magnetic stirrer for 4 h to achieve a 6% (w/v) solution; 10 vol.% AKT was then added to the PCL solution, and the weld samples (10 × 10 × 10 mm) were coated through the immersion method. To this aim, the samples were mechanically polished (up to 1200 grit), degreased, washed with distilled water and dried in hot airflow. The coating process was then carried out on the samples for 10 s, through soaking in the prepared PCL solution. So as to ensure the stability of the composition and viscosity of the solution, the PCL solution was kept in a sealed glassware and hold at a constant temperature of 30 °C using a hot plate and a magnetic stirrer. The samples were withdrawn from the solution with a controlled rate of 3 mm/s and then dried in cool air for 5 min. The final coating was obtained by repeating the mentioned cycle for five times. The samples were labeled as M1, M2 and M3 for the joint without coating, coated using PCL and coated using PCL + 10 wt.% akermanite (PCL-10AKT), respectively.

2.3 Corrosion Tests

Tafel polarization corrosion and electrochemical impedance tests were performed on the welded and coated samples according to the ASTM G59-2017 standard (Ref 48). The test was carried out at 37 °C in a glass vessel containing 250 mL of the SBF solution at pH 7.4 with SBF by the following solutions in 1 L of distilled water: 7.996 g NaCI, 0.350 g $NaHCo_3$, 0.224 g KCI, 0.228 g $K_2HPO_4{\cdot}3H_2O$, 0.305 g $MgCI_2{\cdot}6H_2O$, 0.278 g $CaCI_2$, 0.071 g Na_2SO_4, 6.057 g $NH_2C(CH_2OH)_3$ and 40 cm^3 HCI (Ref 49) by using Potentiostat/Galvanostat Bio-Logic SP300. The saturated calomel reference electrode (SCE) and platinum counter electrode and welded specimens were used as the working electrode with a constant scanning rate of 2 mV/s and an initial value of − 250 mV below the open-circuit potential for 20 min and the size of the exposed surface of 1.7 cm^2.

2.4 Immersion Test

The immersion tests were performed on the untreated, PCL-coated and PCI–AKT-coated samples, according to the ASTM G31-72 standard (Ref 50) using the SBF solution. The samples were prepared with a 1 cm^2 surface area and immersed in 10 mL of SBF which was maintained in a cylindrical container based on the Kokubu instructions:

$$V_s = S_a/10$$

where V_s is the volume of SBF (mL) and S_a is the exposed surface of the sample (mm^2). The time periods for the immersion test were selected to be 72, 168, 336, 504 and 672 h (3 days, and 1, 2, 3 and 4 weeks, respectively). The containers were then put into a water bath of 37 °C temperature. After soaking in SBF for certain periods, the samples were taken out from the SBF and washed with distilled water and finally dried in air. The specimens' weight was measured (the accuracy of 0.001 g), and the results were recorded as the increased weight. The morphology of the samples after soaking for 1 month was investigated via scanning electron microscopy (SEM) equipped with an EDS analyzer. The x-ray diffraction (XRD) test was used for phase analysis via a PHILIPS PW3040 XRD spectrometer (Cu lam, λ = 0.154186 nm). The range of diffraction angle (2θ) was considered as 10°-90°, and the step size and time were determined as 0.02° and 1 s, respectively. Furthermore, the pH variations of the SBF solution through the immersion test period were monitored using a Satrious pH

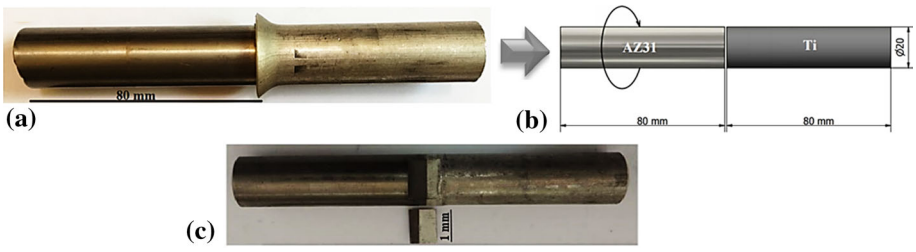

Fig. 1 (a) Workpieces, (b) the coated Ti/AZ31 weld joint and (c) the Ti/AZ31 weld joint prepared samples

meter. It is worth noting that the pH meter was calibrated via standard solutions (pH of 4, 7 and 10) for each test.

2.5 Cellular Tests

Biocompatibility of each sample was investigated through cell morphology test using osteosarcoma cells (MG-63) after 3 and 7 days. In order to determine the cytotoxicity of the samples and its effect on the growth and proliferation of cells, the extracts were prepared based on ISO 10993-5 standard (Ref 51). The cell culture conditions were adjusted by the natural condition of human body (temperature of 37 °C and neutral pH).

To investigate the biocompatibility (cell viability), the indirect extracting test strategy was applied. The first step is to prepare the extract of each sample. Thus, 1 mL of the culture medium for each 5 mg of the sample was added and the specimens were incubated under 95% moisture and 5% CO_2 gas. Then, the medium was taken out in 3- and 7-day periods and loaded by additional cells. A certain content of the culture medium was also considered as the control sample. Again, the cell culture medium conditions were determined similar to those of the normal human body. The cytotoxicity assessment was carried out through the following steps:

(a) At the first step, 1×10^4 cells were seeded in a 96-well plate and incubated for 24 h at 37 °C, which can lead to the attachment of the cells to the bottom of the plate. (b) Each extract was added to the culture well, and the cells were exposed to the mentioned extracts for another 24 h. (c) The culture medium was detached, and 100 µL of colorless RPIM plus 10 µL of MTT solution (molarity of 0.012) was added to each well. (d) After 4 h, the solution was replaced by DMSO to dissolve the violet crystals. (e) The concentration of the dissolved material in RPMI was determined at 545 nm wavelength. Since the optical density (OD) is related to the amount of survived cells, the viability can be determined according to the control sample as follows:

$$CV(\%) = \frac{OD_S}{OD_C} \quad \text{(Eq 1)}$$

where OD_S and OD_C show the mean optical densities of the test samples and the control sample, respectively (Ref 52).

The cells were placed onto the samples in the culture medium for 3 days to evaluate the cells' morphology and adhesion. The culture medium was completely removed after 3 days. Then, using the PBS solution, the specimens were cleaned. Finally, the cultured cells on the samples were stabilized by a 4% formaldehyde solution for 30 min. Then, the stabilizing solution was completely removed and DAPI fluorescent color was added to change the color of the cells' core into blue. Next, the cultured cells were investigated and due images were captured via a fluorescent microscope (Ref 53-55).

Alizarin red staining test was used to measure the amount of precipitated calcium by bone cells in 7 days. The solution was removed after 7 days of culture, the cells were stabilized by 4% formaldehyde solution and then the 1% alizarin red solution (prepared in a Tris buffer with the approximate pH of 8 for 15 min) was added. Finally, the cell-containing well was repeatedly washed with PBS (Ref 56). The morphology of the specimens was then evaluated via an invert optical microscope.

To investigate the alkaline phosphatase (ALP) activity in days 3 and 7 of cell culture on the samples, RIPA solution was initially used to extract the whole protein. The process includes the complete separation of the cell extracts, pouring 20 µL of RIPA solution on them and further pipetage of the samples for 10 min. The RIPA solution was centrifuged for 10 min at the rate of 14,000 rpm and held at 4 °C. Then, for each 20 µL of RIPA solution, 1 mM of reagent No. 1 of commercial ALP kit was added to the samples and incubated for 1 min in an incubator at 37 °C. Next, 250 µL of the solution No. 2 was added and incubated for 1 min in the incubator. After 1, 2 and 3 min, the light absorption was read at a 405 nm wavelength. Then, the difference of light absorption from the previous minute was determined. Finally, these three differences were summed and averaged and the final number was multiplied by factor 3433 (Ref 57).

3. Results and Discussion

3.1 Microstructure

Figure 2(a)–(c) depicts the uncoated CP-Ti/AZ31 sample microstructure. No distinct region can be distinguished on the Ti side, and there is no effect of deformation. However, several regions can be detected in the Mg side including near the weld zone (dynamic recrystallization (DRX)), the base metal and TMAZ or thermomechanically affected zone. The XRD analysis of the weld zone is presented in Fig. 2(d), which indicates that neither the Ti-Mg solid solution nor the intermetallic compounds were formed. However, a reaction can take place between Ti and the aluminum that exists in the magnesium alloy, and as a consequence, different intermetallic compounds such as TiAl, Ti_3Al, and $TiAL_3$ will be generated (Ref 19). As a result of severe deformation and higher temperature in the course of friction welding process, Al can diffuse toward the Ti interface. Since Al-Ti solubility is higher compared with Mg-Al, Ti_3Al can be formed which can be detected in the XRD results. The PCL-coated Ti/AZ31 weld joint surface without AKT has a smooth layer with several pores (Fig. 3a). The formation of pores was principally due to phase separation: the solvent evaporates in the PCL medium and serves as a driving force. Throughout solvent evaporation, the PCL medium is thermodynamically unstable. Consequently, a polymer-rich or a polymer-poor phase will be formed (Ref 8). The latter phase will result in the generation of pores, while the former one might be solidified (Ref 23). This kind of distribution offers adhesion between the polymer layer and magnesium substrate. After incorporating AKT, the PCL film pore structure is reduced and the surface becomes relatively rough with the existence of AKT particles in the composite film (Fig. 3b).

Figure 3(c) shows the cross section of the PCL/AKT-coated Ti/AZ31 weld joint specimens. Deposition of thick and compact layers (54-56 µm) which are uniformly formed on the Mg surface can be observed in this figure. This thick film in the polymer-coated samples works as an obstacle to the dissolution of Mg and is definitely capable of decreasing the corrosion rate (Ref 7). These results also indicate that the thickness of the film is minimally affected by the AKT existence in PLC. However, the film containing AKT showed the presence of Si, Mg and Ca, in addition to C and O (Fig. 3d).

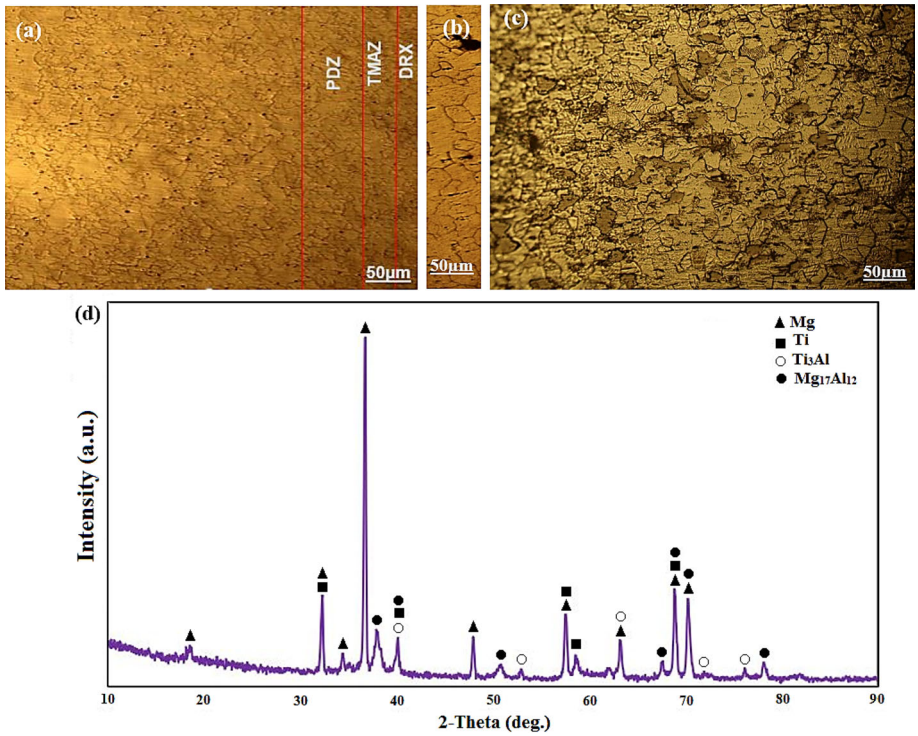

Fig. 2 Optical microscopy image of sample M1: (a) the Mg alloy side, (b) Ti/AZ31 alloy weld zone, (c) the Ti side, (d) XRD results of the weld zone

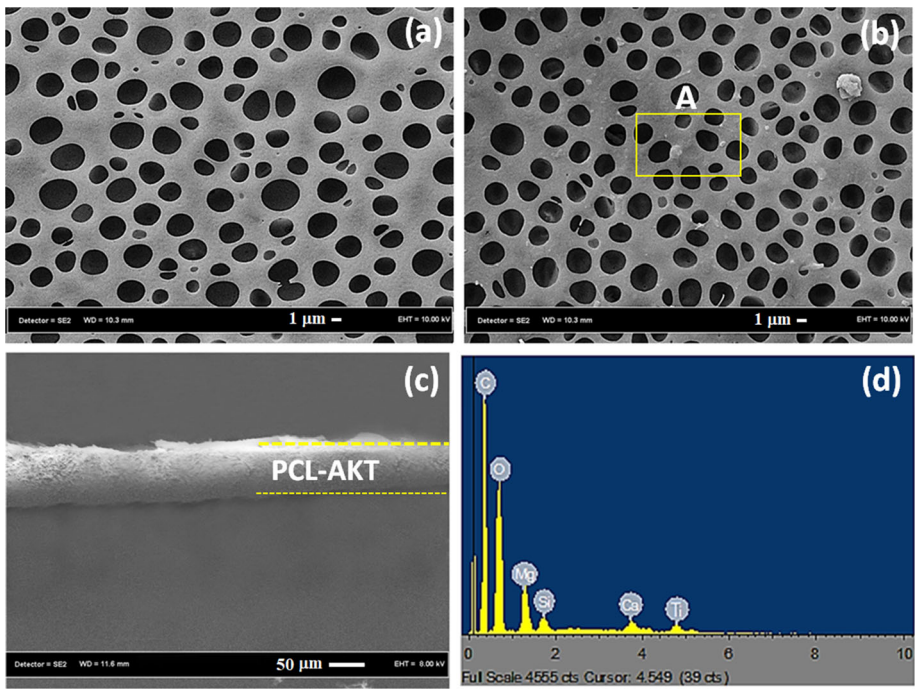

Fig. 3 SEM micrographs of (a) PCL-coated, and (b) PCL–AKT-coated Ti/AZ31 weld joint and (c) cross-sectional SEM micrograph of PCL–AKT-coated Ti/AZ31 weld joint, (d) EDS analysis of Area A

3.2 Immersion Studies

Figure 4(a) shows a schematic of the samples prior to immersion. The findings of the immersion experiments of the untreated and coated Ti/AZ31 weld joint specimens with PCL and PCL with AKT in SBF over a 1-month period are shown in Fig. 4(b) and (c). Figure 4(b) demonstrates the mass percentage changes of the samples by reference to time. As can be seen, with an increase in the solution pH after 7 days, the mass of sample M1 (without coating) decreases rapidly (Fig. 4b, c). After 14 days of soaking, the pH value of the solutions with the uncoated and PCL- and PCK–AKT-coated Ti/AZ31 weld joint

samples varied between 12.8 and 8.7, respectively. During the incubation period, this clearly indicates that the pH increase of the uncoated sample is much greater than the coated sample. Owing to the deposition of the PCL and PCK–AKT layer, the corrosion rate of Ti/AZ31 weld joint reduced.

The pH of the untreated coated Ti/AZ31 weld joint sample is in the range of 7.4 to 12, while the pH of the coated Ti/AZ31 weld joint sample is 8. The flawlessness of the coating is indicated by this constant pH value. Nevertheless, the occurrence of corrosion in the interface is confirmed as some corrosion products can be found in the layer. During the first 3 days of immersion, it can be seen that the uncoated sample's pH value increases to a greater degree compared with that of the coated specimen. The results of mass loss test and pH are in good agreement. This is due to the fact that the highest pH increase is connected to the higher rates of corrosion of the uncoated sample, while the lowest amount of increase was related to the coated samples with less corrosion (Ref 54). Although in the early phases of corrosion the Mg^{+2} and OH^{-} ions formation cannot be totally prevented by the PCL and PCL–AKT coatings, the amount of Mg^{2+} and OH^{-} ions released in the uncoated samples was higher compared to the PCL and PCL–AKT coatings. This significantly increased the pH of the uncoated sample in comparison with the PCL- and PCL–AKT-coated Ti/AZ31 weld joint over time (Ref 58).

Basically, two factors affect the low corrosion resistance of the M1 sample (without coating), the primary galvanic corrosion resulting from the second phase or impurities and the hydroxide layer that is formed on its surface. Magnesium corrosion is based on these general reactions (Ref 34):

$$\text{Anodic reaction: } Mg \rightarrow Mg^{2+} + 2e^{-}$$
$$\text{Cathodic reaction: } 2H_2O + 2e^{-} \rightarrow H_2 + 2OH^{-}$$
$$\text{Final reaction: } Mg + 2H_2O \rightarrow Mg(OH)_2 + H_2$$

In the final reaction, the production of hydrogen raises concern about the creation of gas bubbles during the implantation of magnesium implants into the living tissue. The corrosion products will be deposited on the surface of the sample due to the local increase in the pH value (which is related to rapid Mg degradation). On the basis of mass reduction, the average corrosion rate was determined for the uncoated sample as 15.945 mm/year. Similar calculations were not made for the corrosion rate in the coated piece as the removal of corrosion products without taking the PLC layer off is difficult. Thus, the highest pH increase was in sample M1 (uncoated sample) and the lowest increase in pH was in the coated samples, i.e., M2 (PCL-coated) and M3 (PCL-10AKT-coated).

Since the coated samples' pH values slowly increase in the first 3 days, it can be inferred that chemical dissolution and also improvement in the corrosion resistance of these samples occur at a low speed. During 336 to 720 h of soaking, the pH of the uncoated and coated Ti/AZ31 weld joint samples decreased, which could be due to the deposition of the degradation substances because they consume the hydroxyl groups (OH^{-}) present in the SBF (Ref 59). The main purpose of modifying the levels of magnesium-based biomaterials is to reduce their decomposition or corrosion rates. According to Fig. 4(c), after coating, the corrosion rate has been reduced to about 90%. However, the corrosion of the coated magnesium alloys side decreases but does not stop. During the corrosion process, the existence of defects and cracks can locally increase the substrate corrosion. So, the coating integrity and durability are essential for the Mg-based medical equipment lifetime. This may be associated with the adhesion strength and topography of the coating to the substrate (Ref 39). Figure 5 shows a schematic of how the coating is destroyed during prolonged exposure to the simulated body fluid (SBF). Upon the exposure of the PCL- and PCL–AKT-coated Ti/AZ31 weld joint to the SBF solution, at the beginning of the immersion process, the porous layer of the PLC-based coatings is penetrated by the SBF ions. This results in reduced electrochemical corrosion resistance and formation of a number of cavities. Simultaneously, due to hydrolysis of their ester bonds and acid formation in the surrounding environment, PCL decomposition of acrylamide fibers leads to the Ca^{2+} and Mg^{2+} formation. As a result of increased concentration of Ca^{2+} due to the decomposition of AKT in the surrounding environment, especially in the interface between the solution and the coating layer, the PCL-based coating surface completely takes a negative charge. The

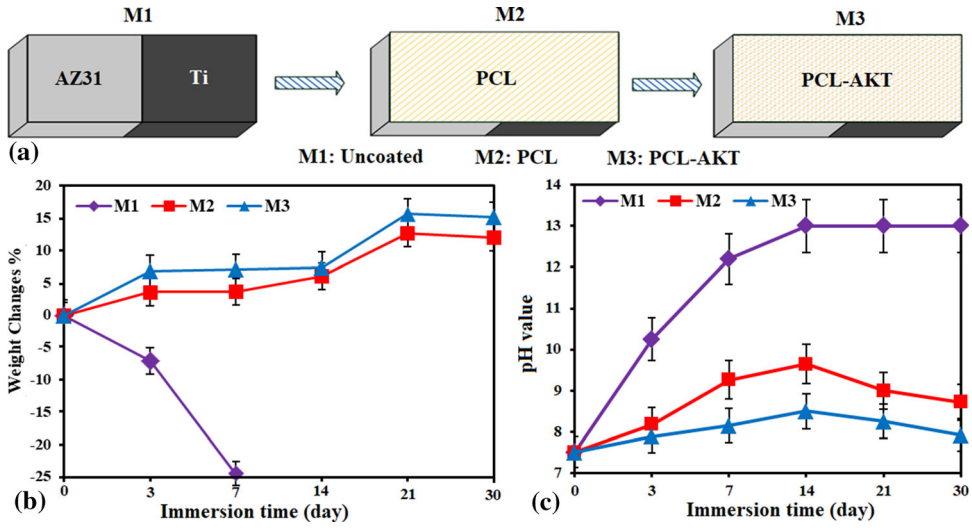

Fig. 4 (a) Schematic of the samples before immersion, (b) weight change, (c) pH change of uncoated Ti/AZ31 weld joint (M1), PCL-coated (M2) and PCL–AKT-coated (M3) Ti/AZ31 weld joint in SBF after 30 days

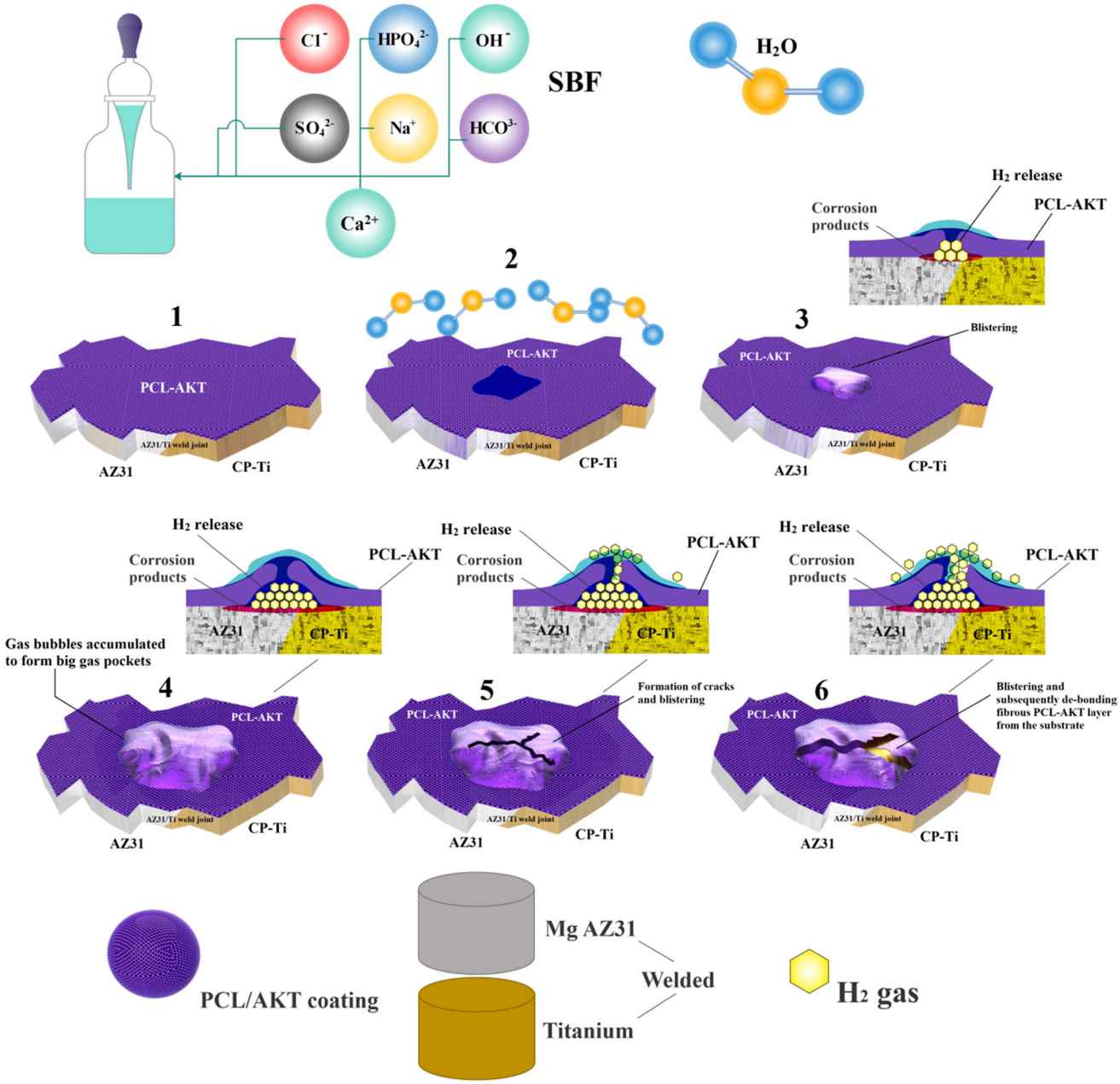

Fig. 5 Schematic illustration of the corrosion mechanism of the PCL–AKT-coated Ti/AZ31 weld joint after immersion in the SBF solution

Ca^{2+} and Mg^{2+} ions are absorbed in this environment. As a result, the whole surface takes a positive charge since the positively charged ions are deposited. Subsequently, the ions with negative charge, i.e., OH^-, PO_4^{3-} and CO_3^{2-}, are deposited on the surface. Due to the existence of OH^- and the gathering of PO_4^{3-} and Ca^{2+} ions calcium phosphate (apatite) will be formed on the coating layer surface (Ref 58).

The polymer-coated Ti/AZ31 weld joint specimen corrosion consists of an intricate blend of one or more procedures: Polymers such as PCL experience a combination of surface and volumetric degradation in SBF. If the surface bonds' hydrolysis failure rate is quicker than liquid diffusion into the polymer volume, erosion or degradation will occur, leading to a thinner coating. In volumetric degradation, on the contrary, as water rapidly penetrates into the whole polymer volume, the ester bonds in the volume will accidentally break. An escalation in the amount of carboxyl groups (COOH–) formed as a result of ester bond breakage raises its acid content. Penetration of the COOH– groups into the solution around it leads to the degradation of material from inside. Making a distinction between the degradation types within the PCL layer on the magnesium sample is difficult. Due to the polymer layer degradation, the simulator solution penetrates into the metal surface and subsequently corrosion occurs (Ref 39). The acidic pH that is a resultant of degradation can influence the substrate corrosion rate. The solution pH change results from the polymer degradation. Differentiating these factors in the coated sample is difficult.

Figure 6(a) shows the comparison of the XRD pattern of the samples. The amount of secondary phases in the samples is below the XRD detection limit. $Mg(OH)_2$ peaks were detected in all samples. After immersion in the simulator solution,

samples M2 and M3 (coated samples) show $Mg(OH)_2$, $Mg_3Ca_3(PO_4)_4$ and $Ca_2(P_4O_{12})\cdot 4H_2O$ peaks for 30 days, indicating that they are formed as corrosion substances (Ref 60). The formation of aforesaid peaks indicates that the material is bioactive. These products are easily traceable in the polymer layer and in the PCL–AKT and PCL-coated samples.

Figure 6(b) shows the FTIR spectra of samples M1 (uncoated), M2 (PCL-coated) and M3 (PCL-10AKT-coated). In sample M1, the OH characteristic peaks are detected at 3697 and 1643 cm^{-1}, CO_3^{2-} peaks at 1643 and 1502 cm^{-1} and PO_4^{3-} peaks at 1277, 1094, 557 and 458 cm^{-1}, respectively. In sample M2, PCL has the commonest typical peaks of C=O stretching vibration at 1719 cm^{-1}, $-CH_2$ asymmetric stretching vibration at 2932 cm^{-1}, $-CH_2$ symmetric stretching vibration at 2860 cm^{-1} and C-O stretching vibration at 1159 cm^{-1}. $-CH_2$ bending vibration is identified at 1466 cm^{-1} (asymmetric) and 1234 cm^{-1} (symmetric). After AKT addition into the PCL (sample M3), a peak appears at 475 cm^{-1} corresponding to the Mg-O bond. The peaks at 928 and 886 cm^{-1} are related to the Si-O stretching vibration (Ref 48). In addition, the peak stretching vibrations were C=O at 1719 cm^{-1}, asymmetric stretching vibration $-CH_2$ at 2922 cm^{-1}, $-CH_2$ symmetric tensile vibration at 2857 cm^{-1}, and C-O tensile vibration at 1159 cm^{-1}.

Figure 7 shows the samples EDS spectra and SEM microscopy after the uncoated sample immersion in SBF (after 7 days) and PCL- and PCL–AKT-coated samples (after 30 days). Extensive surface cracking accompanied by pitting corrosion can be observed in the uncoated alloy. However, compared to uncoated specimen, both the PCL- and PCL–AKT-coated samples experienced a milder, more uniform corrosion attack. On the bare and coated samples surfaces, a large amount of corrosion products with cauliflower morphology accumulated, as can be seen in the high-magnification image. The EDS results (from Mg side) show that the PCL- and PCL–AKT-coated samples have great quantities of P, Mg, Ca and O in the corrosion products. One of the essential components of bone, Ca and P, has been reported to form a calcium phosphate layer (Ca/P atomic ratio is 1.25-1.64) on the PCL and PCL–AKT coatings after SBF immersion (Ref 61, 62). The ability of the PCL- and PCL–AKT-coated specimens to form a hydroxyapatite layer on their surfaces indicates their high capability for bone formation after soaking in SBF.

3.3 Electrochemical Studies

Figure 8(a) shows the Nyquist plots (Z' in Z'') of the PCL–AKT- and PCL-coated Ti/AZ31 weld joint specimens. As can be seen, the frequency escalates counterclockwise, so the points close to the origin of the coordinates will find the highest frequency. According to Fig. 8(a), two loops are seen in most of the curves, one at high frequencies (left) associated with the coating and the other at low frequencies (right) that transmit the charge in the metal/electrolyte interface. The increase in the diameter of these two rings is interpreted to increase the corrosion resistance of the system (Ref 63). According to the Nyquist plots shown in Fig. 8(a), it is clear that the curve for sample M3 (PCL–AKT) and then sample M2 (PCL) has the highest total resistance. It is worth observing that the semicircle diameter of the M1 sample is much smaller than that of the M2 and M3 samples. There is an induction for the coated polymer sample. The diameter of the high- and medium-frequency rings indicates the surface heterogeneity and the porous layer charge transfer resistance on the surface. In the case of uncoated alloys, this applies to surface corrosion products, while for the coated samples, this is due to the polymer coating (Ref 36).

The PCL-coated sample presented greater charge transfer resistance, R_{ct}, compared with the bare sample, indicating a positive influence of the PCL coating on the corrosion resistance of the substrate (Ref 58). A simple equation was used to evaluate the samples as shown in Fig. 8(b). In the equivalent circuit shown in Fig. 8, R_{sol} is the solution resistance and R_{ct} and Q_2 are the load transfer resistance of the double layer and the fixed phase element of the double layer, respectively. In addition, R_1 and Q_1 signify the resistor and the constant phase elements of the coating, respectively. In this circuit, instead of the ideal capacitor, the constant phase element is utilized. R_{ct} for the M1 (uncoated), M2 (PCL), and M3 (PCL–AKT) samples are 5357 ± 43, 7809 ± 52 and $11{,}842 \pm 51\ \Omega\ cm^2$, respectively. Because of the existence of a shielding layer on the surface of the alloy, the uniformity of the coating layer and the uniform distribution of AKT in the PCL film resulted in a significant increase in R_{ct}. This designates that the PCL–AKT layer can increase the substrate corrosion resistance (Ref 58). The presence of AKT in the PCL coating, even as agglomerated particles, leads to the creation of a steady protecting coating which escalates the Ti/AZ31 weld joint corrosion resistance. Therefore, the corrosion resistance of the

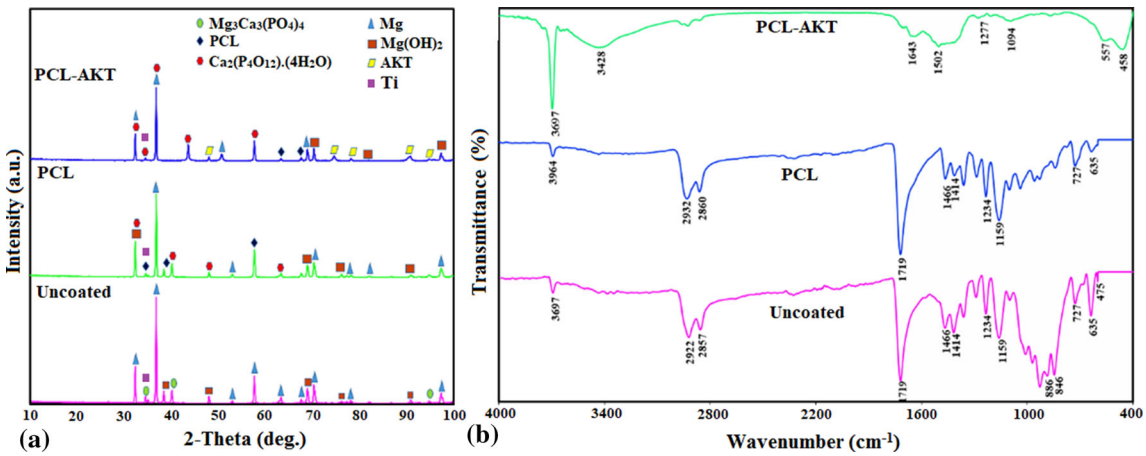

Fig. 6 (a) The x-ray diffraction patterns and (b) FTIR analysis of the uncoated, PCL- and PCL–AKT-coated samples after immersion in the SBF solution for 30 days

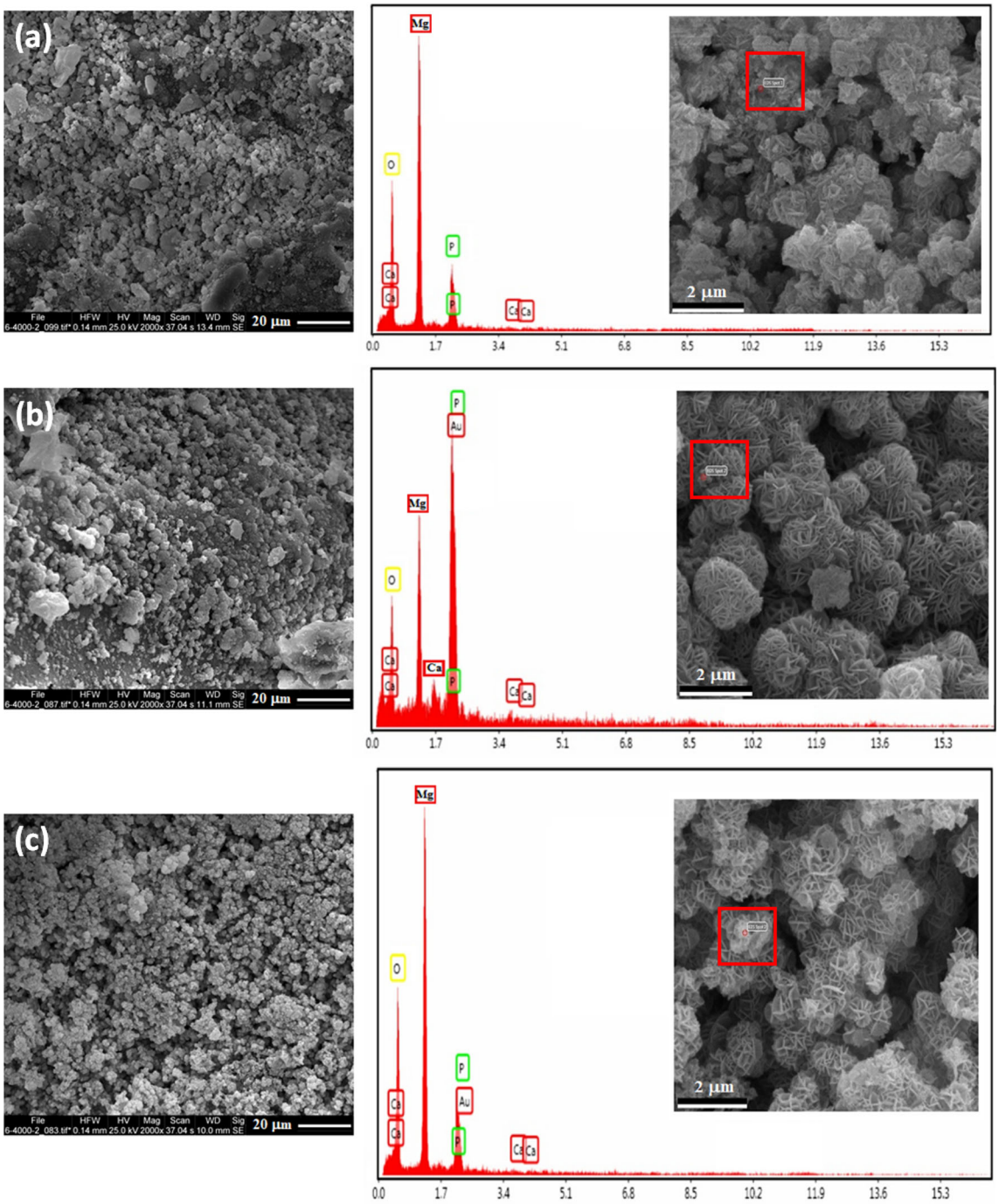

Fig. 7 SEM micrographs and corresponding EDS analysis of (a) the uncoated; (b) PCL-coated and (c) PCL–AKT-coated specimens after immersion in the SBF solution for 30 days

Ti/AZ31 weld joint, in particular magnesium alloy side, seems to be associated with the obstacle influence of ceramic–organic (PCL–AKT) and the coating/substrate interface-augmented adhesion strength as a result of chemical bonding that greatly prevents the soluble penetration into the substrate (Ref 58). Another representation of the EIS test data that can provide useful information for system analysis is the Bode plots. On one side of these plots, the impedance modulus ($\sqrt{(Z'^2 + Z''^2)}$ represented as |Z|) is plotted in terms of frequency logarithms. On the other side of them, the phase angle symmetry (− Arc tan (Z''/Z')) is plotted in terms of frequency logarithms. The advantage of this method over Nyquist plots is that the values of the frequencies are known from the diagram.

Figure 8(c) shows the Bode plots of the PCL–AKT- and PCL-coated Ti/AZ31 weld joint specimens. The Bode plots demonstrate the overall resistance of the system (Ref 64-67). Thus, according to Fig. 8(c), it is observed that the impedance at the lowest frequency of the M2 (PCL) and M3 (PCL–AKT) samples is higher compared with the uncoated Ti/AZ31 weld joint sample. This confirms previous results concerning that the coating specimens' corrosion resistance is greater and the lower impedance at the lower frequency of sample M1 is also evident,

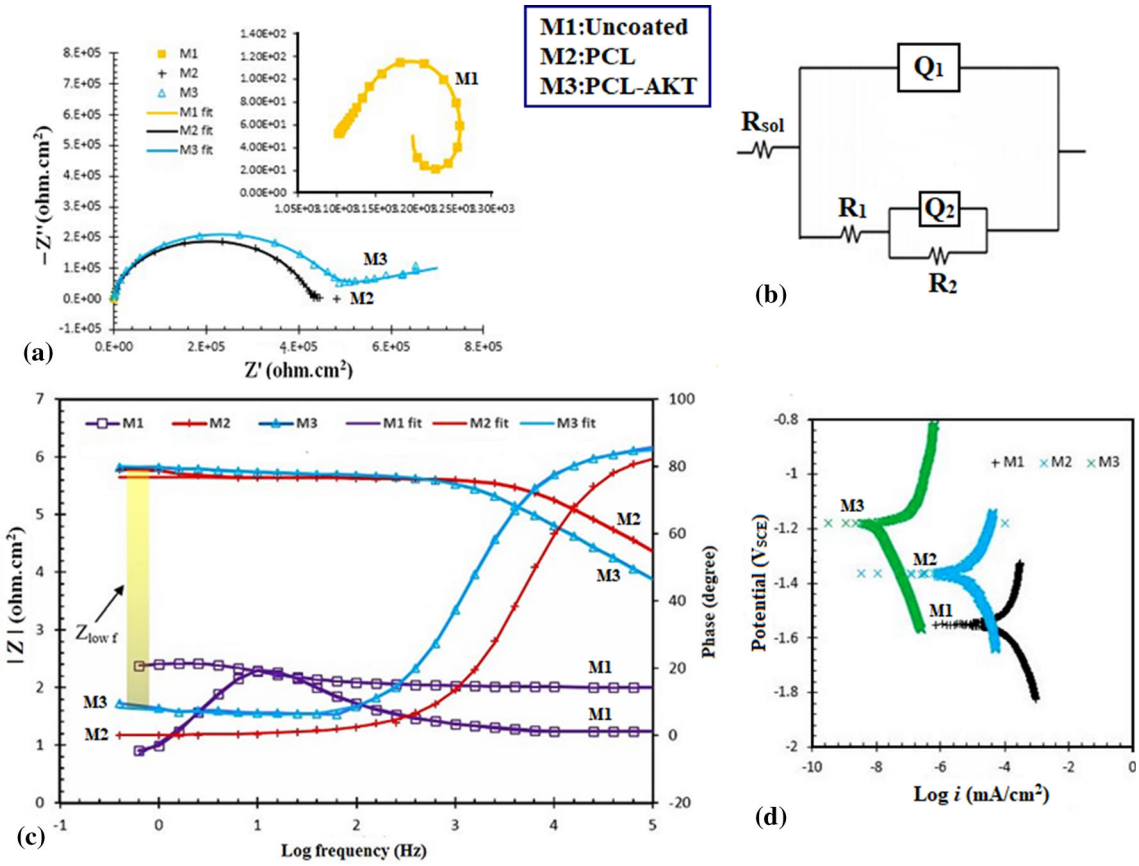

Fig. 8 (a) Nyquist plots, (b) equivalent electrical circuit for the uncoated and coated samples, (c) bode magnitude plot and Bode phase plot, (d) potentiodynamic polarization curves of the uncoated Ti/AZ31 weld joint (M1), PCL (M2)- and PCL–AKT-coated Ti/AZ31 weld joint (M3) in SBF

representing a significant reduction in the corrosion resistance of the system in this specimen. Although the impedance at the lowest frequency is about 5.5 to 6 Ω cm^2 for the M2 and M3 samples, respectively, this value is about 5 Ω cm^2 for sample M1 (uncoated). In addition, at most frequencies, the phase angle is about 80° to 90° for the coated samples, while it is about 0 for the uncoated sample. All of these results show that the corrosion resistance of the bare system is very low in comparison with the coated system.

Figure 8(d) shows that the Ti/AZ31 weld joint coated with PCL had a higher E_{corr} (− 1.38 V_{SCE}) and a lower i_{corr} (0.0019 μA/cm^2) compared with the uncoated Ti/AZ31 weld joint (E_{corr} = − 1.55 V_{SCE} and i_{corr} = 0.05 μA/cm^2). Compared with the coated samples, the negative corrosion potential is greater for the uncoated sample due to the creation of a micro-galvanic cell in the magnesium sample (Ref 64). As can be seen, compared to the i_{corr} of the M2 (PCL) and M3 (PCL–AKT) specimens, the i_{corr} of sample M1 (uncoated) is significantly lower, indicating the lower corrosion rate of the two coated specimens which is because of the barrier effect of PCL-based film. As such, the AKT-PCL coating layer acts as an anode barrier, reducing the penetration of SBF into the substrates and preventing galvanic corrosion. In addition, compared to the uncoated sample, the barrier layer leads to a more positive corrosion potential (Ref 58). Due to their fundamental effect on blocking cavities, the presence of ceramic mineral particles increases the protection against the corrosion of the PCL coatings. It should be noted that the uncoated and coated Ti/AZ31 weld joint specimens were soaked in SBF (for OCP) for 30 min so that a constant corrosion occurred. Throughout this period, great amounts of corrosion products were formed on the coating layer which played the role of a barrier to inhibit the departure of more ions from the substrate. Simultaneously, these products decreased the penetration of corrosive materials into the substrate and protected the substrate (Ref 58). In this regard, the presence of AKT nanoparticles in the PCL coating layer might cause fast apatite formation from the SBF solution. Owing to this deposition, the AKT-PCL layer showed a constant corrosion (Ref 58). The values of the electrochemical parameters of each sample are comparable in the analysis table.

The obtained results are demonstrated in Table 1. β_a and β_c are the anodic and cathodic slopes, respectively. E_{corr} (V_{SCE}) is the sample corrosion potential of the samples, i_{corr} is the corrosion current density and R_p is the polarization resistance. The specimens polarization resistance is obtained as follows:

$$R_P = \frac{\beta_a \beta_c}{2.3(\beta_a + \beta_c) i_{corr}} \quad \text{(Eq 2)}$$

According to the results of polarization diagrams, the polarization resistance of M2 (PCL-coated) and M3 (PCL–AKT-coated) specimens is higher than the other ones. The corrosion potentials of the bare and coated specimens are reported in Table 1. Thermodynamically, the corrosion potential is related to the tendency for corrosion. The more negative the corrosion potential of a system, the greater the thermodynamic tendency of the system to corrode. In other words, the

alloy is more active in the corrosive environment under study. According to Table 1, the coating samples corrosion potential is more positive than the uncoated sample, indicating a less thermodynamic tendency for the sample to corrode.

3.4 Cell Response

Figure 9(a)–(c) shows the fluorescent microscope images of the cultured cells on the samples for 3 days. As can be observed, the cell nucleus stained with fluorescent dye DAPI is seen in blue. According to Fig. 9, the number of cells bound to the surface of the coated Ti/AZ31 weld joint (M2 and M3) specimens is greater than the uncoated (M1) specimen. In addition, the number of cells adhering to PCL–AKT coating increased significantly. Previous studies have shown that due to the presence of elements such as calcium, magnesium and silicon, AKT with the chemical formula $Ca_2MgSi_2O_7$ had essential role in cell growth and proliferation (Ref 45-47). Due to the rapid deposition of apatite, the addition of AKT to the PCL coating layer may create a favorable environment on the coating surface. The presence of calcium in the AKT ($Ca_2MgSi_2O_7$) inside PCL film can promote good cell attachment and subsequently improve bone formation (Ref 58).

Figure 9(d) shows the cell viability chart of extracts on days 3 and 5. As can be seen, cell viability increased at all the time points in the sample coated with PCL–AKT (M3). However, after 7 days, cell viability increased significantly, with the survival rate for the PCL–AKT (M3) reaching 97.52%. The results of cell viability are quite consistent with those of cell adhesion. These findings depicted that the embedding of AKT to the PCL coating enhances biocompatibility. The production of some ions, such as Si, Ca and Mg, from the AKT encapsulated in the PCL coating is able to offer an appropriate environment regarding living bone cells (Ref 58). As can be seen, cell viability for the uncoated and coated samples increases with the time of culture.

Table 1 Electrochemical parameters of specimens in SBF solution attained from the polarization test

Sample	β_a, v.dec^{-1}	$-\beta_c$, v.dec^{-1}	E_{corr} SCE, V	i_{corr}, µA/cm^2
Uncoated (M1)	0.2	0.21	− 1.56	18.2
PCL (M2)	0.37	0.40	− 1.38	0.3
PCL–AKT (M3)	0.09	0.10	− 1.16	0.01

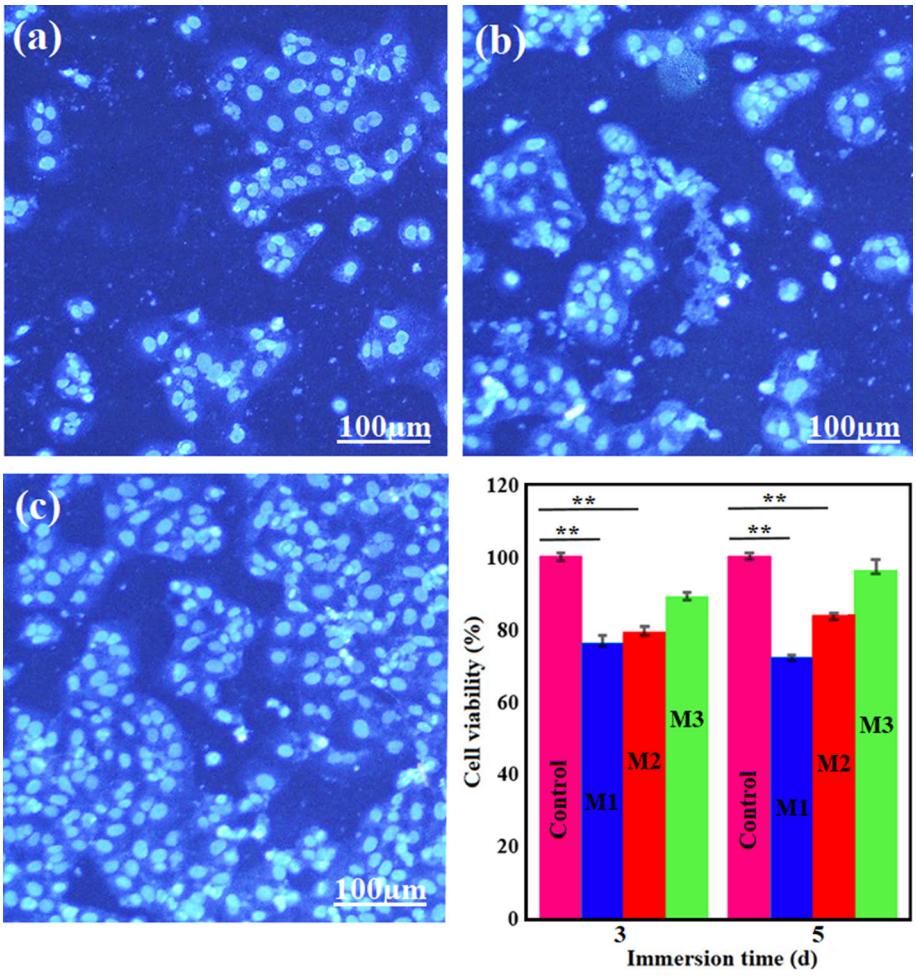

Fig. 9 DAPI staining of MG63 osteoblasts cells on (a) the uncoated, (b) PCL-coated, (c) PCL–AKT-coated Ti/AZ31 weld joint, (d) cell viability of MG63 osteoblast cells after incubation in the uncoated and coated Ti/AZ31 weld joint for 3 and 5 days. Note: uncoated (M1), PCL (M2) and PCL–AKT (M3)

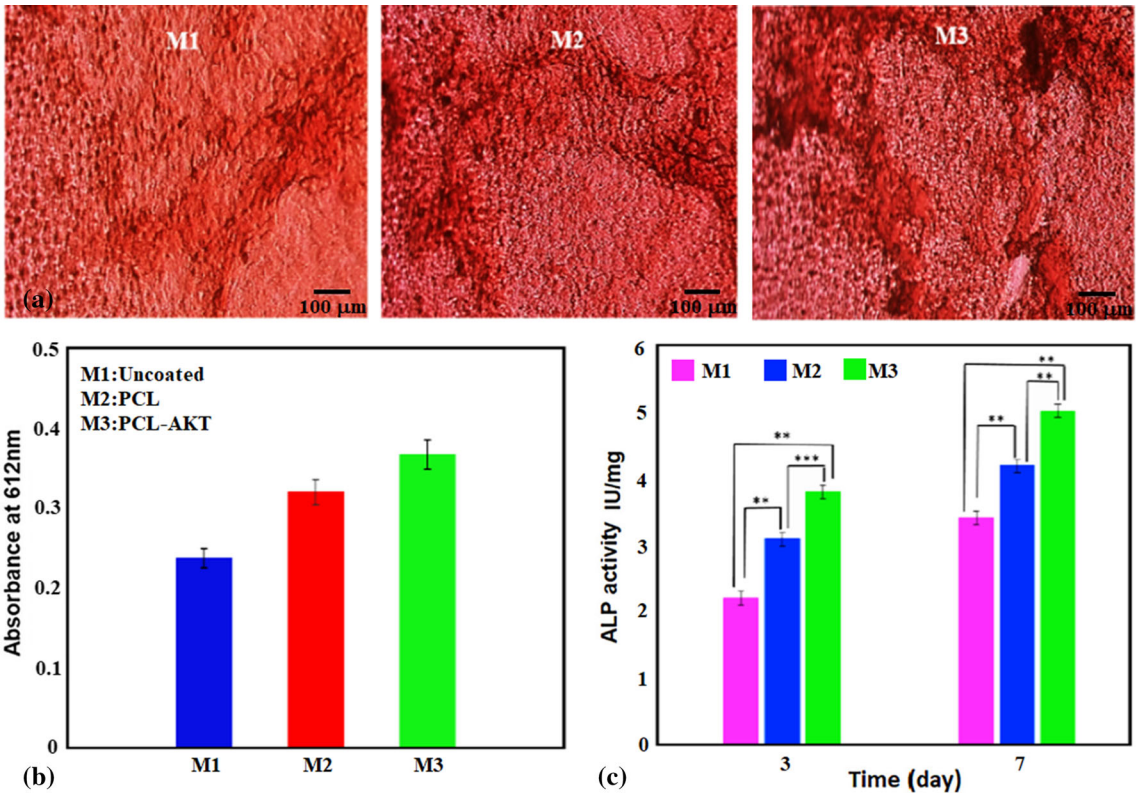

Fig. 10 Alizarin red staining of MG-63 cells cultured on (a) the uncoated, PCL-coated, PCL–AKT coated, (b) OD values and (c) ALP of MG-63 cells cultured on the uncoated, PCL-coated and PCL–AKT-coated Ti/AZ31 weld joint for 3 and 7 days. Note: uncoated (M1), PCL (M2) and PCL–AKT (M3)

Figure 10 shows the results of cellular tests including alizarin red stain (a), alizarin red stain absorption spectrum (b) and alkaline phosphatase activity (c) of uncoated (M1), PCL (M2) and PCL–AKT (M3) samples. These findings are likewise in agreement with the previous outcomes including biocompatibility and cell adhesion, with osteogenic activity of the specimens significantly increasing in the PCL–AKT (M3). This amount of osteogenesis activity for the uncoated (M1) sample is drastically reduced. Alizarin red is a commonly employed dye to exhibit mineralization or the ability of a cell to produce calcium. Figure 10(a) and (b) shows the staining of alizarin in the cells. Calcium deposition is detectable as dark red streaks in light microscope images. In this perspective, Ti/AZ31 weld joint sample coated with PCL–AKT (M3), the deposition of calcium was significantly increased, and the light absorption of the samples was also increased.

Alkaline phosphatase (ALP) is an endocrine enzyme that has an essential role in accelerating the dephosphorylation process of proteins and nucleic acids and is found in important body tissues, especially in the bone. The activity of this enzyme reflects the function of tissues. Figure 10(c) shows the results of the evaluation of ALP on 3 and 7 days. According to the images, the activity of alkaline phosphatase enzyme up to 7 days was higher for the coated sample in comparison with for untreated specimens. According to the previous studies (Ref 68-70), the cell culture process consists of three stages: (1) cell proliferation and growth associated with an increase in the number of cells, (2) increasing collagen secretion and reaching the highest level, (3) decreasing collagen secretion and initiation of calcium deposition, increasing the mineralization process. According to the figure, the enzyme activity is higher in the coated samples containing AKT, which indicates the effect of this enzyme on the induction of bone cell activity. The results of ALP test are well supported by other tests and indicate the role of AKT in the PCL layer in osteogenesis induction.

Compared to the PCL coatings (M2), PCL coatings encapsulating AKT (M3) depicted a considerably greater ALP activity. In addition, the results show that the ALP activity of the coated Ti/AZ31 weld joint sample increases with the time of cultivation. This is owing to the dissolution of the AKT ion products, which resulted in greater cellular binding and growth (Ref 58). Furthermore, provision of PCL-based coating on Ti/AZ31 weld joint surface reduces magnesium ions production from the substrate by forming a PCL-based protective film. This reduces the corrosion rate of the magnesium alloy side in Ti/AZ31 weld joint and subsequently improves its biocompatibility. Therefore, application of PCL–AKT on the surface of Ti/AZ31 weld joint seems to escalate ALP activity as the soaking time increases, which means great bioactivity. Owing to the generation of soluble ionic products (Ca and Si) from the AKT present in PCL, the positive role of PCL–AKT film in cell viability and adhesion is confirmed (Ref 58).

4. Conclusion

(1) The uncoated Ti/AZ31 weld joint microstructure showed that no titanium region was detectable on the titanium side and no titanium side shape was observed. On the

magnesium side, various regions including near welding zones, i.e., DRX and TMAZ as well as the base metal area, are observed. Also, the PCL–AKT coating was more uniformly applied to the specimens due to the good distribution of AKT in the coating.

(2) The highest increase in corrosion and pH value for the uncoated Ti/AZ31 weld joint sample (M1) was because of magnesium high solubility in aqueous media. During the first 72 h, a sluggish escalation in the pH value of the coated Ti/AZ31 weld joint samples indicates a slow chemical dissolution and improved corrosion resistance. During 336 to 720 h of immersion, the pH of the coated samples decreased, which could be because of the degradation products deposition on the surface.

(3) Due to the presence of AKT in the PCL film with elements such as calcium, magnesium and silicon, the PCL–AKT-coated Ti/AZ31 weld joint sample has higher cell adhesion and cell viability (97.52%).

(4) The alizarin red staining and ALP activity show that in the Ti/AZ31 weld joint sample coated with PCL–AKT, the osteogenic activity was significantly increased.

References

1. X. Li, X. Liu, S. Wu, K.W.K. Yeung, Y. Zheng, and P.K. Chu, Design of Magnesium Alloys with Controllable Degradation for Biomedical Implants: From Bulk to Surface, *Acta Biomater.*, 2016, **45**, p 2–30
2. F. Witte, V. Kaese, H. Haferkamp, E. Switzer, A. Lindenberg, C.J. Wirth, and H. Windhagen, In Vivo Corrosion of Four Magnesium Alloys and the Associated Bone Response, *Biomaterials*, 2005, **17**, p 3557–3563
3. M. Razzaghi, M. Kasiri-Asgarani, H.R. Bakhsheshi-Rad, and H. Ghayour, In Vitro Degradation, Antibacterial Activity and Cytotoxicity of Mg-3Zn-xAg Nanocomposites Synthesized by Mechanical Alloying for Implant Applications, *J. Mater. Eng. Perform.*, 2019, **28**, p 1441–1455
4. H.R. Bakhsheshi-Rad, E. Hamzah, S. Farahany, and M. Staiger, The Mechanical Properties and Corrosion Behavior of Quaternary Mg-6Zn-0.8Mn-xCa Alloys, *J. Mater. Eng. Perform.*, 2015, **24**(2), p 598–608
5. L. Xu, G. Yu, E. Zhang, F. Pan, and K. Yang, In Vivo Corrosion Behavior of Mg-Mn-Zn Alloy for Bone Implant Application, *Biomed. Mater. Res. A*, 2007, **83**, p 703–711
6. C. Janning, E. Willbold, C. Vogt, J. Nellesen, A. Meyer-Lindenberg, H. Windhagen, F. Thorey, and F. Witte, Magnesium Hydroxide Temporarily Enhancing Osteoblast Activity and Decreasing the Osteoclast Number in Periimplant Bone Remodeling, *Acta Biomater.*, 2010, **6**, p 1861–1868
7. F. Witte, The History of Biodegradable Magnesium Implants: A Review, *Acta Biomater.*, 2010, **6**, p 1680–1692
8. A.M. Khorasani, M. Goldberg, E.H. Doeven, and G. Littlefair, Titanium in Biomedical Applications Properties and Fabrication: A Review, *Biomater. Tissue Eng.*, 2015, **5**, p 593–619
9. M. Balasubramanian, R. Kumar, and S. Gopinath, Multi-Objective Optimisation of Friction Welding Parameters in Joining Titanium Alloy and Stainless Steel with a Novel Interlayer Geometry, *Adv. Mater. Process. Technol.*, 2019, **6**, p 25–39
10. M. Singh, C.E. Smith, R. Asthana, and A.L. Gyekenyesi, Active Metal Brazing of Graphite Foam-to-Titanium Joints Made with SiC-Coated Foam, *Eur. Ceram. Soc.*, 2019, **39**, p 1–9
11. M. Singh, R. Asthana, and T.P. Shpargel, Brazing of Ceramic-Matrix Composites to Ti and Hastealloy Using Ni Base Metallic Glass Interlayers, *Mater. Sci. Eng. A*, 2008, **498**, p 19–30
12. M. Singh, G.N. Morscher, T.P. Shpargel, and R. Asthana, Active Metal Brazing of Titanium to High-Conductivity Carbon-Based Sandwich Structure, *Mater. Sci. Eng. A*, 2008, **498**, p 31–36
13. G.N. Morscher, M. Singh, T. Shpargel, and R. Asthana, A Simple Test to Determine the Effectiveness of Different Braze Compositions for Joining Ti-Tubes to C/C Composite Plates, *Mater. Sci. Eng. A*, 2006, **418**, p 19–24
14. T. Ozaki, Y. Hasegawa, H. Tsuda, S. Mori, M.C. Halbig, M. Singh, and R. Asthana, TEM Analysis of Interfaces in Diffusion-Bonded Silicon Carbide Ceramics Joined Using Metallic Interlayers, in *Advanced Processing and Manufacturing Technologies for Nanostructured and Multifunctional Materials III*, 2017, vol 37, p 49–55
15. M. Singh, T. Matsunaga, H.T. Lin, R. Asthana, and T. Ishikawa, Microstructure and Mechanical Properties of Joints in Sintered SiC Fiber-Bonded Ceramics Brazed with Ag-Cu-Ti Alloy, *Mater. Sci. Eng. A*, 2012, **557**, p 69–76
16. M.C. Halbig, R. Asthana, and M. Singh, Diffusion Bonding of SiC fibeR-Bonded Ceramics using Ti/Mo and Ti/Cu Interlayers, *Ceram. Int.*, 2015, **41**, p 2140–2149
17. M. Singh and R. Asthana, Characterization of Brazed Joints of CAC Composite to Cu-Clad-Molybdenum, *Compos. Sci. Technol.*, 2008, **68**, p 3010–3019
18. M.C. Halbig, B.P. Coddington, R. Asthana, and M. Singh, Characterization of Silicon Carbide Joints Fabricated using SiC Particulate-Reinforced Ag-Cu-Ti Alloys, *Ceram. Int.*, 2013, **39**, p 4151–4162
19. A. Lakshminarayanan, R. Saranarayanan, V.K. Srinivas, and B. Venkatraman, Characteristics of Friction Welded AZ31B Magnesium–Commercial Pure Titanium Dissimilar Joints, *Magn. Alloys*, 2015, **3**(3), p 315–321
20. W. Li, A. Vairis, M. Preuss, and T. Ma, Linear and Rotary Friction Welding Review, *Int. Mater. Rev.*, 2016, **61**(2), p 1–30
21. P. Rombaut, W. De Waele, and K. Faes, Friction welding of steel to ceramic, *Sustain Constr Des.*, 2011, **2**(3), p 448–457
22. M.M. Attallah, M. Preuss, C. Booncharoen, A. Steuwer, J.E. Daniels, D.J. Hughes, C. Dungey, and G.J. Baxter, Microstructural and Residual Stress Development Due to Inertia Friction Welding in Ti-6246, *Metall. Mater. Trans. A*, 2012, **9**, p 3149–3161
23. F. Witte, N. Hort, C. Vogt, S. Cohen, K.U. Kainer, R. Willumeit, and F. Feyerabend, Degradable Biomaterials Based on Magnesium Corrosion, *Curr. Opin. Solid State Mater. Sci.*, 2008, **12**, p 63–72
24. T.S.N.S. Narayanan, I.S. Park, and M.H. Lee, Strategies to Improve the Corrosion Resistance of Microarc Oxidation (MAO) Coated Magnesium Alloys for Degradable Implants: Prospects and Challenges, *Prog. Mater. Sci.*, 2014, **60**, p 1–71
25. A. Zomorodian, M.P. Garcia, T. Moura e Silva, J.C.S. Fernandes, M.H. Fernandes, and M.F. Montemor, Biofunctional Composite Coating Architectures Based on Polycaprolactone and Nanohydroxyapatite for Controlled Corrosion Activity and Enhanced Biocompatibility of Magnesium AZ31 Alloy, *Mater. Sci. Eng. C*, 2015, **48**, p 434–443
26. Y. Ding, C. Wen, P. Hodgson, and Y. Li, Effects of Alloying Elements on the Corrosion Behavior and Biocompatibility of Biodegradable Magnesium Alloys: A Review, *Mater. Chem. B*, 2014, **2**, p 1912–1933
27. Y. Sun, B. Zhang, Y. Wang, L. Geng, and X. Jiao, Preparation and Characterization of a New Biomedical Mg-Zn-Ca Alloy, *Mater. Des.*, 2012, **34**, p 58–64
28. W. Zhang, M. Li, Q. Chen, W. Hu, W. Zhang, and W. Xin, Effects of Sr and Sn on Microstructure and Corrosion Resistance of Mg-Zr-Ca Magnesium Alloy for Biomedical Applications, *Mater. Des.*, 2012, **39**, p 379–383
29. H.R. Bakhsheshi-Rad, E. Hamzah, M. Medraj et al., Effect of Heat Treatment on the Microstructure and Corrosion Behaviour of Mg-Zn Alloys, *Mater. Corros.*, 2014, **65**, p 999–1006
30. J.R. Smith and D.A. Lamprou, Polymer Coatings for Biomedical Applications: A Review, *Surf. Eng. Coat.*, 2014, **92**, p 9–19
31. S. Abela and F. Czerwinski, Ed., *Protective Coatings for Magnesium Alloys*, InTech, Rijeka, 2011
32. D.B. Prabhu, P. Gopalakrishnan, and K.R. Ravi, Coatings on Implants: Study on Similarities and Differences Between the PCL Coatings for Mg Based Lab Coupons and Final Components, *Mater. Des.*, 2017, **135**, p 397–410
33. S. Ehtemam-Haghighi, K.G. Prashanth, H. Attar, A.K. Chaubey, G.H. Cao, and L.C. Zhang, Evaluation of Mechanical and Wear Properties of Ti-xNb-7Fe Alloys Designed for Biomedical Applications, *Mater. Des.*, 2016, **111**, p 592–599
34. A.K. Nasution and H. Hermawan, *Degradable Biomaterials for Temporary Medical Implants, Biomaterials and Medical Devices*, Springer, Berlin, 2016, p 127–160

35. M. Vert, Degradable and Bioresorbable Polymers in Surgery and in Pharmacology :Beliefs and Facts, *Mater. Sci.: Mater. Med.*, 2009, **20**, p 437–446
36. Y. Chen, Y. Song, S. Zhang, J. Li, C. Zhao, and X. Zhang, Interaction Between a High Purity Magnesium Surface and PCL and PLA Coatings During Dynamic Degradation, *Biomed. Mater.*, 2011, **6**, p 1–8
37. X.N. Gu, Y.F. Zheng, Q.X. Lan, Y. Cheng, Z.X. Zhang, T.F. Xi, and D.Y. Zhang, Surface Modification of an Mg-1Ca Alloy to Slow Down Its Biocorrosion by Chitosan, *Biomed. Mater.*, 2009, **4**, p 1–8
38. C. Wu, Z. Wen, C. Dai, Y. Lu, and F. Yang, Fabrication of Calcium Phosphate/Chitosan Coatings on AZ91D Magnesium Alloy with a Novel Method, *Surf. Coat. Technol.*, 2010, **204**, p 3336–3374
39. B. Li and T. Webster, *Orthopedic Biomaterials Advances and Applications*, Springer, New York, 2017
40. L.Y. Li, L.Y. Cui, R.C. Zeng, S.Q. Li, X.B. Chen, Y. Zheng, and M.B. Kannan, Advances in Functionalized Polymer Coatings on Biodegradable Magnesium Alloys: A Review, *Acta Biomater.*, 2018, **79**, p 23–36
41. N. Siddiqui, S. Asawa, B. Birru, R. Baadhe, and S. Rao, PCL-based composite scaffold matrices for tissue engineering applications, *Mol. Biotechnol.*, 2018, **60**(7), p 506–532
42. M.A. Woodruff and D.W. Hutmacher, The Return of a Forgotten Polymer-Polycaprolactone in the 21st Century, *Prog. Polym. Sci.*, 2010, **35**, p 1217–1256
43. H.M. Wong, P.K. Chu, F.K.L. Leung, K.M.C. Cheung, K.D.K. Luk, and K.W.K. Yeung, Engineered Polycaprolactone-Magnesium Hybrid Biodegradable Porous Scaffold for Bone Tissue Engineering, *Mater. Int.*, 2014, **24**, p 561–567
44. H.R. Bakhsheshi-Rad, A.F. Ismail, M. Aziz, M. Akbari, Z. Hadisi, S.M. Khoshnava, E. Pagan, and X. Chen, Co-Incorporation of Graphene Oxide/Silver Nanoparticle into Poly-L-Lactic Acid Fibrous: A Route Toward the Development of Cytocompatible and Antibacterial Coating Layer on Magnesium Implants, *Mater. Sci. Eng. C*, 2020, **111**, p 110812
45. A. Liu, M. Sun, X. Yang, C. Ma, Y. Liu, X. Yang, S. Yan, and Z. Gou, Three-Dimensional Printing Akermanite Porous Scaffolds for Load-Bearing Bone Defect Repair: An Investigation of Osteogenic Capability and Mechanical Evolution, *Biomater. Appl.*, 2016, **31**, p 650–660
46. K. Marzban, S.M. Rabiee, E. Zabihi, and S. Bagherifard, Nanostructured Akermanite Glass–Ceramic Coating on Ti6Al4V for Orthopedic Applications, *Appl. Biomater. Funct. Mater.*, 2018, **17**, p 1–8
47. L. Xia, Z. Yin, L. Mao, X. Wang, J. Liu, X. Jiang, Z. Zhang, K. Lin, J. Chang, and B. Fang, Akermanite Bioceramics Promoteosteogenesis, Angiogenesis and Suppress Osteoclastogenesis For osteoporotic Bone Regeneration, *Sci. Rep.*, 2016, **6**, p 1–17
48. American Society for Testing and Materials (ASTM), *Standard Test Method for Conducting Potentiodynamic Polarization Resistance Measurements*, ASTM International, West Conshohocken, 2017
49. A. Nasution, M.F. Ulum, M.R. Abdul Kadir, and H. Hermawan, Mechanical and Corrosion Properties of Partially Degradable Bone Screws made of Pure Iron and Stainless Steel 316L by Friction Welding, *Sci. China Mater.*, 2018, **61**, p 593–606
50. American Society for Testing and Materials (ASTM), *Standard Practice for Laboratory Immersion Corrosion Testing of Metals*, ASTM International, West Conshohocken, 2017
51. International Standard (ISO), *Biological Evaluation of Medical Devices Part 5, Tests for In Vitro Cytotoxicity*, ISI, Geneva, 2009
52. H.R. Bakhsheshi-Rad, E. Hamzah, S. Bagheriyan, M. Daroonparvar, M. Kasiri-Asgarani et al., Preparation and Performance of Plasma/Polymer Composite Coatings on Magnesium Alloy, *J. Mater. Eng. Perform.*, 2016, **25**(9), p 3948–3959
53. H.R. Bakhsheshi-Rad, E. Hamzah, A.F. Ismail, M. Aziz, Z. Hadisi, M. Kashefian, and A. Najafinezhad, Novel Nanostructured Baghdadite-Vancomycin Scaffolds: In-Vitro Drug Release, Antibacterial Activity and Biocompatibility, *Mater. Lett.*, 2017, **209**, p 369–372
54. S. Liu, H. Liu, Z. Yin, K. Guo, and X. Gao, Cytotoxicity of Pristine C60 Fullerene on Baby Hamster Kidney Cells in Solution, *Biomater. Nanobiotechnol*, 2012, **3**(3), p 385–390
55. H.R. Bakhsheshi-Rad, E. Hamzah, N. Abbasizadeh et al., Synthesis of Novel Nanostructured Bredigite–Amoxicillin Scaffolds for Bone Defect Treatment: Cytocompatibility and Antibacterial Activity, *J. Sol-Gel. Sci. Technol.*, 2018, **86**(1), p 83–93
56. F.Y. Cao, W.N. Yin, J.X. Fan, R.X. Zhuo, and X.Z. Zhang, A Novel Function of BMHP1 and cBMHP1 Peptides to Induce the Osteogenic Differentiation of Mesenchymal Stem Cells, *Biomater. Sci.*, 2015, **3**(2), p 345–351
57. S. Wang, Z. Gu, Z. Wang, X. Chen, L. Cao, L. Cai, Q. Li, J. Wei, J.W. Shin, and J. Su, Influences of Mesoporous Magnesium Calcium Silicate on Mineralization, Degradability, Cell Responses, Curcumin Release from Macro–Mesoporous Scaffolds of Gliadin Based Biocomposites, *Sci. Rep.*, 2018, **8**(1174), p 1–12
58. H.R. Bakhsheshi-Rad, M. Akbari, A.F. Ismail, M. Aziz et al., Coating Biodegradable Magnesium Alloys with Electrospun Poly-L-Lactic Acid-Akermanite-Doxycycline Nanofibers for Enhanced, *Surf. Coat. Technol.*, 2019, **377**, p 1–14
59. Y. Song, S. Zhang, J. Li, C. Zhao, and X. Zhang, Electrodeposition of Ca-P Coatings on Biodegradable Mg Alloy: In Vitro Biomineralization Behavior, *Acta Biomater.*, 2010, **6**, p 1742–1763
60. E. Ziyaei, M. Atapour, H. Edris, and A. Hakimizad, Corrosion Behavior of PEO Coatings Formed on AZ31 Alloy in Phosphate-Based Electrolytes with Calcium Acetate Additive, *Mater. Eng. Perform.*, 2017, **26**, p 3204–3215
61. P. Feng, P. Wu, C. Gao, Y. Yang, W. Guo, W. Yang, and C. Shuai, A Multimaterial Scaffold with Tunable Properties: Toward Bone Tissue Repair, *Adv. Sci.*, 2018, **5**(4), p 1–15
62. Y. Sasikumar, A. Madhan Kumar, R. Suresh Babu, P. Dhaiveegan, N. Al-Aqeeli, and A.L.F. Barros, Fabrication of Brushite Coating on AZ91D and AZ31 Alloys by Two-Step Chemical Treatment and Its Surface Protection in Simulated Body Fluid, *Mater. Eng. Perform.*, 2019, **28**, p 3803–3815
63. S. Arthanari and K.S. Shin, A Simple One Step Cerium Conversion Coating Formation on to Magnesium Alloy and Electrochemical Corrosion Performance, *Surf. Coat. Technol.*, 2018, **349**, p 757–772
64. V. Shkirskiy, A.D. King, O. Gharbi, P. Volovitch, J.R. Scully, K. Ogle, and N. Birbilis, Revisiting the Electrochemical Impedance Spectroscopy of Magnesium with Online Inductively Coupled Plasma Atomic Emission Spectroscopy, *Chem. Phys. Chem.*, 2014, **16**(3), p 536–539
65. M. Daroonparvar, M.A.M. Yajid, N.M. Yusof, H.R. Bakhsheshi-Rad et al., Improvement of Corrosion Resistance of Binary Mg-Ca Alloys Using Duplex Aluminum-Chromium Coatings, *J. Mater. Eng. Perform.*, 2015, **24**(7), p 2614–2627
66. H.R. Bakhsheshi-Rad, E. Hamzah, H.Y. Tok, M. Kasiri-Asgarani et al., Microstructure, In Vitro Corrosion Behavior and Cytotoxicity of Biodegradable Mg-Ca-Zn and Mg-Ca-Zn-Bi Alloys, *J. Mater. Eng. Perform.*, 2017, **26**(2), p 653–666
67. S. Saud, E. Hamzah, T. Abubakar, H.R. Bakhsheshi-Rad, et al., Effects of Mn Additions on the Structure, Mechanical Properties, and Corrosion Behavior of Cu-Al-Ni Shape Memory Alloys, *J. Mater. Eng. Perform.*, 2014, **23**, p 3620–3629
68. H.R. Bakhsheshi-Rad, E. Hamzah, M.R. Abdul-Kadir et al., The Mechanical Properties and Corrosion Behavior of Double Layered Nano Hydroxyapatite-Polymer Coating on Mg-Ca Alloy, *Mater. Eng. Perform.*, 2015, **24**, p 4010–4021
69. H.R. Bakhsheshi-Rad, E. Hamzah, A.F. Ismail et al., Synthesis and In Vitro Performance of Nanostructured Monticellite Coating on Magnesium Alloy for Biomedical Applications, *J. Alloys Compd.*, 2019, **773**, p 180–193
70. Y. Huang, X. Jin, X. Zhang, H. Sun, J. Tu, T. Tang, J. Chang, and K. Dai, In Vitro and In Vivo Evaluation of Akermanite Bioceramics for Bone Regeneration, *Biomaterials*, 2009, **30**(28), p 5041–5048